

Gyro-kinetic simulation of global turbulent transport properties in tokamak experiments

W. X. Wang, Z. Lin,^{a)} W. M. Tang, W. W. Lee, S. Ethier, J. L. V. Lewandowski, G. Rewoldt, T. S. Hahn, and J. Manickam

Plasma Physics Laboratory, Princeton University, P. O. Box 451, Princeton, New Jersey 08543

(Received 23 January 2006; accepted 31 July 2006; published online 11 September 2006)

A general geometry gyro-kinetic model for particle simulation of plasma turbulence in tokamak experiments is described. It incorporates the comprehensive influence of noncircular cross section, realistic plasma profiles, plasma rotation, neoclassical (equilibrium) electric fields, and Coulomb collisions. An interesting result of global turbulence development in a shaped tokamak plasma is presented with regard to nonlinear turbulence spreading into the linearly stable region. The mutual interaction between turbulence and zonal flows in collisionless plasmas is studied with a focus on identifying possible nonlinear saturation mechanisms for zonal flows. A bursting temporal behavior with a period longer than the geodesic acoustic oscillation period is observed even in a collisionless system. Our simulation results suggest that the zonal flows can drive turbulence. However, this process is too weak to be an effective zonal flow saturation mechanism. © 2006 American Institute of Physics. [DOI: 10.1063/1.2338775]

I. INTRODUCTION

Understanding turbulence and associated transport in toroidal plasmas^{1–3} is one of the key issues in magnetic fusion research. In the past decade, as computer resources rapidly increased and advanced, numerical algorithms were developed, and significant progress was made for this long-standing complicated issue through computer simulation based on various approaches.^{4–15} Among them, the first-principles based gyro-kinetic particle approach¹⁶ has been widely employed. Simulation studies carried out with the gyro-kinetic toroidal code (GTC)⁸ have been among the most productive. GTC was originally developed to focus on fundamental nonlinear turbulence physics. It is a full-torus global code using a global field-line-following mesh and a real space field solver. Global turbulence simulations for toroidal plasmas are highly demanding for the following reasons: (i) the turbulence-generated zonal flow contains radial scales as large as the system size, even though the turbulence itself is on the much smaller scale of the gyro-radius; (ii) the equilibrium $\mathbf{E} \times \mathbf{B}$ shear flow, which also plays an important role in determining turbulence levels, typically has the large scale size of the plasma minor radius; and (iii) turbulence spreading to the linearly stable zone results in nonlocal transport, which is a truly global phenomenon. To pose the simplest problem while keeping the important global physics properties, a simplified model was utilized in the previous simulations, with simple magnetic geometry with a large-aspect-ratio circular concentric cross section and neglect of the effect of radial variation of pressure. This proved to be an effective means of gaining basic insights into the complexity of the toroidal turbulence system. As a result, the previous simulation studies have led to a number of important understandings with regard to zonal flow effects, transport scalings

with collisionality and device size, turbulence spreading, etc.^{8,17–21} While such a simplified model is a useful tool to separate and clarify fundamental physics issues, more realistic features are needed as the research moves forward. Particularly for simulating turbulence phenomena in tokamak experiments, a more comprehensive model is needed that consistently incorporates the influence of general geometry, realistic plasma profiles, plasma flow, neoclassical equilibrium, Coulomb collisions and other features. In this paper we present such a model with emphasis on the general geometry capability, which has now been implemented based on GTC architecture. The general geometry simulation capability has been interfaced with TRANSP,²² a widely used experimental data analysis software tool for specifying experimental plasma profiles of temperature, density and toroidal angular velocity, and also with various numerical magnetohydrodynamic (MHD) equilibrium codes, including the JSOLVER²³ and ESC²⁴ codes.

Global turbulence fluctuation levels and associated transport are determined by both local and nonlocal physics. Turbulence propagation in the radial direction results in transport nonlocality which should be addressed by global simulation. The new capability is applied to shaped plasmas with DIII-D²⁵ geometry to examine the ion temperature gradient (ITG) turbulence spreading phenomena and the global turbulence evolution process. We also investigate the nonlinear interplay between turbulence and zonal flow, which is essentially a local process. As an attempt to understand the nonlinear zonal flow dissipation, which is needed to saturate zonal flow and to explain the mutual self-regulation observed in collisionless simulations, we study the process of zonal flow driving turbulence. Our simulation results suggest that the coupling of zonal flows to turbulence and associated energy transfers are much weaker, compared to the opposite process in ITG turbulence.

The rest of the paper is organized as follows. The gen-

^{a)}Present address: Department of Physics and Astronomy, University of California, Irvine, CA 92697.

eral geometry simulation model is described in Sec. II. We describe the coordinate system and mesh construction, with consideration of shaped equilibrium geometry and strong nonuniformity of the global temperature profile; we detail the calculation of the gyro-kinetic transformation of fluctuations between particle position and guiding center position in generalized geometry; the system of basic gyro-kinetic equations used in this generalized simulation model is also presented. Our simulation results are presented in Sec. III. These include linear and nonlinear ITG benchmarks in a simple geometry, global turbulence evolution in a DIII-D-shaped plasma, and turbulence self-regulation in collisionless plasma. Concluding remarks are summarized in Sec. IV.

II. GENERAL GEOMETRY GYRO-KINETIC PARTICLE SIMULATION MODEL

A. Coordinate system and mesh construction

Magnetic flux coordinates, in which the radial coordinate labels magnetic surfaces, are generally used for toroidal systems and associated with MHD equilibria. Our gyro-kinetic simulation in principle can use arbitrary flux coordinates with straight field lines. In the flux coordinates, the global field-line-following mesh, which possesses the highest efficiency by capturing the flute-type character of the drift wave turbulence in toroidal plasmas, can be easily constructed. A preferable flux coordinate can be chosen in terms of different requirements. A symmetric coordinate system in which the toroidal angle φ is chosen to be the azimuthal angle of cylindrical coordinates is preferable in many cases. These coordinates are relatively uniform compared to others that have been previously used, and are advantageous for constructing a relatively regular mesh in real space for strongly shaped plasmas. It also facilitates straightforward visualization with the poloidal plane defined with the physical angle φ . The radial coordinate is defined as $r = \sqrt{\psi/\psi_e}$, where ψ and ψ_e are the toroidal flux and its value on the plasma boundary, respectively. This same radial coordinate is widely used in the experimental community.

Because of the flute-type character of drift wave turbulence in toroidal plasmas, with $k_{\parallel} \ll k_{\perp}$, where k_{\parallel} and k_{\perp} are the parallel and perpendicular wave numbers, respectively, GTC uses a field-line-following mesh, which shows high efficiency for calculating the turbulent field. Note that the field-line-following mesh does not possess toroidal symmetry. On the other hand, in tokamak geometry, the toroidal symmetry is broken as fluctuations associated with microinstability develop. Each mode nonlinearly sees an asymmetric equilibrium that consists of the MHD equilibrium, which is symmetric, and the fluctuations of other modes, which are asymmetric. In our simulation, the MHD equilibrium is represented by a two-dimensional (2-D) symmetric mesh, and the fluctuations are represented using a (toroidally nonsymmetric) field-line-following mesh that best represents the nature of the mode structure. For drift wave turbulence, the spatial scale length in the perpendicular direction is generally in correlation with the local gyro-radius $\rho_j \propto \sqrt{T_j}$, which may vary substantially from the core to the edge of the plasma. For instance, it is common in National Spherical Torus

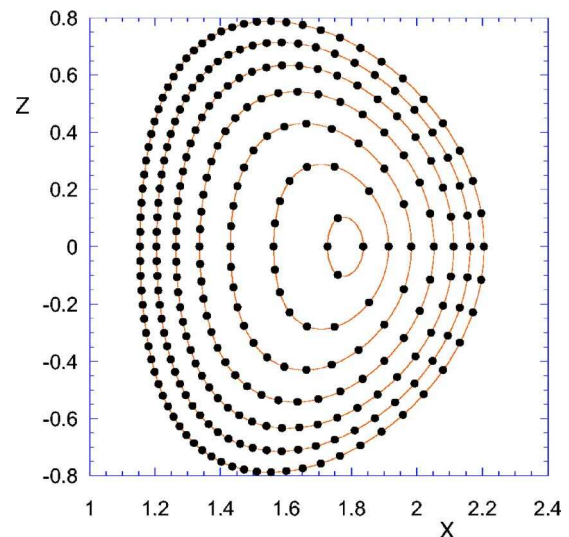


FIG. 1. (Color online) An example of a nonuniform grid on a poloidal plane showing grid size in correlation with local ion gyro-radius.

Experiment (NSTX)²⁶ plasmas that the ion temperature changes from \sim keV in the core to \sim 10 eV near the separatrix region at the plasma edge. Therefore, for a global simulation, which includes the entire radial domain, it is important to use a nonuniform grid with the grid size in the perpendicular direction correlated with the local gyro-radius for improved spatial resolution and efficiency. To this end, we rescale the radial coordinate by defining ρ as follows:

$$\frac{d\rho}{dr} = \sqrt{T_c/T_i(r)}, \quad (1)$$

where T_c is the temperature at a reference radial location. Working with the new coordinate ρ , we use an evenly spaced radial grid, which offers great convenience for frequent operations such as particle sorting, charge deposition, gathering, etc. This allows the grid size in real space to be correlated with the local gyro-radius: $\Delta r \sim \sqrt{T_i(r)/T_c}$. In the poloidal direction, the grid size $\Delta\theta(r)$ is determined so as to make the poloidal arc length Δl_θ near the midplane correlated with ρ . An example of such a grid on the poloidal plane $\varphi=0$ is shown in Fig. 1. Generally, a two-dimensional mesh on the $\varphi=0$ plane is set up first. A three-dimensional mesh is constructed by following each (approximate) field line, which starts at a grid point on the $\varphi=0$ plane and has $\bar{q}(r)\theta - \varphi = \text{constant}$, with \bar{q} slightly changed from the usual safety factor $q(r)$, so that the approximate field lines will lead back to one of the grid points on the $\varphi=0$ plane. Two methods for enforcing toroidal periodicity have been implemented. One method is to map the grid at $\zeta=0$ to the grid at $\zeta=2\pi$ using interpolation, which results in some spatial damping. Another method is to allow the grid to depart slightly from the magnetic field lines in order to match the grid points, which requires a chain rule in calculating the parallel derivatives. Interpolation and deposition, which transfer information between particles and grid points, are performed within a “flux-tube type” of cell twisted along the field line rather than a toroidally symmetric

cell. This has advantages due to separating the short spatial scale in the perpendicular direction and the long spatial scale in the parallel direction. In the field-line-following mesh system, the number of “toroidal grids” (i.e., the number of poloidal planes) is actually the number of grids in the parallel direction within one toroidal circuit. In our simulation, the number of toroidal grids N_t is chosen to give adequate resolution for the parallel structure of the modes. In the perpendicular direction, adequate resolution is achieved by using a much denser mesh on each poloidal plane with a perpendicular grid size of ρ_i scale. The allowed maximum toroidal wave-number is related to both the toroidal and poloidal grids. The key point is that the poloidal mesh makes a significant contribution to the resolution in the toroidal direction. This problem was addressed in detail by Scott.²⁷ Basically, the maximum toroidal mode number that can be resolved is $n = \text{NINT}(m/q) + N_t/2$ for each poloidal mode number m , where $\text{NINT}(m/q)$ is the nearest integer to m/q , and $N_t/2$ is the so called “toroidal Nyquist number.” Therefore, adequate resolution is also guaranteed in the toroidal direction.

Note that the field-line-following mesh described above is used only for calculating fluctuations. A separate 2-D mesh in the same coordinate system with a uniform grid in both the radial and poloidal directions is used to represent the axisymmetric MHD equilibria numerically. This mesh has a larger grid size, as the equilibrium scale length is much larger than that of the turbulence. Multidimensional spline interpolation is used to obtain equilibrium quantities at any spatial location.

The gyro-kinetic particles are followed in general flux coordinates using guiding center Lagrangian equations, instead of Hamiltonian equations that require construction of canonical variables²⁸ that are complicated forms in general geometry and are inconvenient to use. The guiding center Lagrangian obtained by Littlejohn has the following normalized form:^{28,29}

$$L(\mathbf{x}, \dot{\mathbf{x}}; t) = (\mathbf{A} + \rho_{\parallel} \mathbf{B}) \cdot \mathbf{v} - H, \quad (2)$$

with the guiding center Hamiltonian $H = \rho_{\parallel}^2 B^2 / 2 + \mu B + \Phi$. Here, the magnetic field $\mathbf{B} = \nabla \times \mathbf{A}$, $\rho_{\parallel} = v_{\parallel} / B$ is the parallel gyro-radius, μ is the magnetic moment, and Φ is the electric potential. The independent variables are $\mathbf{x} = (r, \theta, \varphi, \rho_{\parallel})$. The particle guiding drift motion is governed by the Lagrangian equations

$$\frac{d}{dt} \left(\frac{\partial}{\partial \dot{x}_i} L \right) - \frac{\partial}{\partial x_i} L = 0. \quad (3)$$

The obtained equations for $d\mathbf{x}/dt$ are suitable for any generalized flux coordinates.

B. Gyro-kinetic transformation

One of the important elements of the gyro-kinetic formalism^{16,30–34} is concerned with the transformation of fluctuations between the particle position \mathbf{x} and the guiding center position \mathbf{R} . The fluctuations, such as the potential ϕ

and the ion density δn_i , in the two coordinates are connected by the gyro-kinetic transformation, which is expressed as follows:

$$\bar{\phi}(\mathbf{R}, \mu) = \frac{1}{2\pi} \int \phi(\mathbf{x}) \delta(\mathbf{x} - \mathbf{R} - \boldsymbol{\rho}) d\mathbf{x} d\Theta, \quad (4)$$

$$\begin{aligned} \bar{\phi}(\mathbf{x}) &= \frac{1}{2\pi} \int \bar{\phi}(\mathbf{R}, \mu) f_{Mi}(\mathbf{R}, \mu, v_{\parallel}) \\ &\times \delta(\mathbf{R} - \mathbf{x} + \boldsymbol{\rho}) d\mathbf{R} d\mu dv_{\parallel} d\Theta, \end{aligned} \quad (5)$$

$$\delta \bar{n}_i(\mathbf{x}) = \frac{1}{2\pi} \int \delta f_i(\mathbf{R}, \mu, v_{\parallel}) \delta(\mathbf{R} - \mathbf{x} + \boldsymbol{\rho}) d\mathbf{R} d\mu dv_{\parallel} d\Theta, \quad (6)$$

where $\boldsymbol{\rho}$ is the gyro-radius vector, Θ is the gyro-phase, f_{Mi} is assumed to be Maxwellian, and δf_i is the perturbed ion distribution function. In a gyro-kinetic simulation, the quantities are calculated either in real space or in Fourier space. In real space, the transformation is carried out by the four-point averaging scheme.³⁵ The exact gyro-average is performed on a gyro-plane perpendicular to the magnetic field, with four points evenly spaced on a gyro-orbit. Because the grid points on which fluctuations ϕ and δn_i that are calculated are set up on poloidal planes, it is much more convenient to perform the gyro-average on poloidal planes instead of on gyro-planes. In the case of the simple geometry of large-aspect-ratio circular concentric cross section, the difference between a poloidal plane and a gyro-plane is neglected in doing the gyro-average. An accurate treatment for the gyro-average in general geometry is obtained by taking into account the finite ratio of the poloidal to the total magnetic field B_p/B , which separates the poloidal plane from the gyro-plane. By projection to the poloidal plane, a gyro-orbit becomes an elliptic orbit (Fig. 2). In the direction of $(\nabla \varphi \times \mathbf{B}) \times \nabla \varphi$, the gyro-radius is elongated by a factor of $1/\cos \alpha$ while there is no change in the $\nabla \varphi \times \mathbf{B}$ direction. Here, $\cos \alpha = \mathbf{B} \cdot \nabla \varphi / B |\nabla \varphi| = \psi' / \mathcal{J} B |\nabla \varphi|$, with $\psi' \equiv d\psi/dr$ and the Jacobian $\mathcal{J} = (\nabla r \times \nabla \theta \cdot \nabla \varphi)^{-1} > 0$ (right handed). The four points used for the gyro-average are chosen to be located on the axes $(\nabla \varphi \times \mathbf{B}) \times \nabla \varphi$ and $\nabla \varphi \times \mathbf{B}$. An ion spends approximately the same amount of time on each quarter of the ellipse. To locate the positions of the four points relative to the guiding center, we first calculate the directional derivatives in the two directions, which are defined as $dA/dl \equiv \hat{\mathbf{l}} \cdot \nabla A$ for any function A , where $\hat{\mathbf{l}}$ is the unit vector in direction \mathbf{l} . In the $\nabla \varphi \times \mathbf{B}$ direction,

$$\frac{dr}{dl_1} = \frac{[(g^{r\varphi})^2 - g^{\varphi\varphi} g^{rr}] / q + g^{rr} g^{\theta\varphi} - g^{r\varphi} g^{r\theta}}{\sqrt{g^{\varphi\varphi} B^2 / \psi'^2 - 1 / \mathcal{J}^2}}, \quad (7)$$

$$\frac{d\theta}{dl_1} = \frac{[g^{\varphi\theta} g^{r\varphi} - g^{\varphi\varphi} g^{\theta\varphi}] / q + g^{r\theta} g^{\theta\varphi} - g^{r\varphi} g^{\theta\theta}}{\sqrt{g^{\varphi\varphi} B^2 / \psi'^2 - 1 / \mathcal{J}^2}}; \quad (8)$$

in the $(\nabla \zeta \times \mathbf{B}) \times \nabla \zeta$ direction,

$$\frac{dr}{dl_2} = - \frac{g^{r\varphi}}{\mathcal{J} \sqrt{g^{\varphi\varphi} \sqrt{g^{\varphi\varphi} B^2 / \psi'^2 - 1 / \mathcal{J}^2}}}, \quad (9)$$

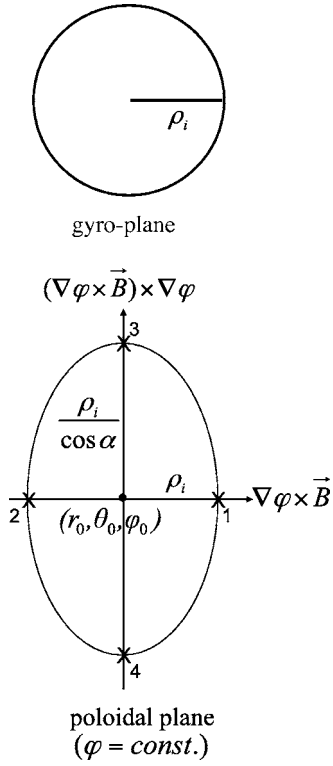


FIG. 2. (Color online) Ion gyro-orbit.

$$\frac{d\theta}{dl_2} = \frac{g^{\varphi\varphi}/q - g^{\theta\theta}}{\mathcal{J}\sqrt{g^{\varphi\varphi}g^{\varphi\varphi}B^2/\psi'^2 - 1/\mathcal{J}^2}}, \quad (10)$$

where the metric tensor $g^{\alpha\beta} = \nabla\alpha \cdot \nabla\beta$. The four points used for the ion gyro-average are determined by

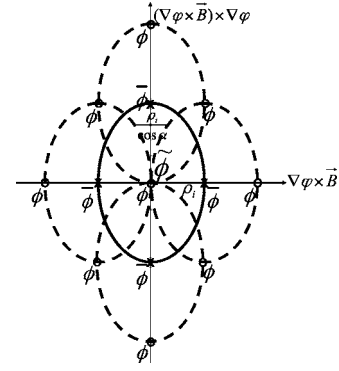
$$r_j = r_0 + \Delta r_j, \quad \theta_j = \theta_0 + \Delta\theta_j, \quad \varphi_j = \varphi_0, \quad j = 1, 2, 3, 4 \quad (11)$$

with

$$\begin{aligned} \Delta r_{1,2} &= \pm \frac{dr}{dl_1} \rho_i, & \Delta\theta_{1,2} &= \pm \frac{d\theta}{dl_1} \rho_i, \\ \Delta r_{3,4} &= \pm \frac{dr}{dl_2} \frac{\rho_i}{\cos\alpha}, & \Delta\theta_{3,4} &= \pm \frac{d\theta}{dl_2} \frac{\rho_i}{\cos\alpha}. \end{aligned} \quad (12)$$

The calculation of the potential $\tilde{\phi}(\mathbf{x})$ in terms of $\phi(\mathbf{x})$ involves the double averaging process.³⁶ Following the above method, we can extend the previous calculation of $\tilde{\phi}(\mathbf{x})$ to general geometry, taking into account finite B_θ/B . The double average is made along the elliptic orbit projected on the poloidal plane as shown in Fig. 3, where $\tilde{\phi}$ at the center point is the four-point average of $\tilde{\phi}$ on the X points, which are other four-point averages of ϕ on the O points. The average over the distribution function is accomplished by carefully sampling different gyro-radii.³⁶

It is noted that the four-point averaging scheme is accurate for $k_\perp \rho_i \leq 2$ modes. To resolve shorter wavelength modes, we may use more points for the averaging process. An implicit assumption of the four-point averaging scheme described above is that the equilibrium scale lengths L_p and

FIG. 3. (Color online) Schematic diagram of double average process for calculating $\tilde{\phi}$ at the center position.

L_B of the pressure and magnetic field are much larger than the ion gyro-radius, which is consistent with the gyro-kinetic ordering.

C. Basic equations

The gyro-kinetic particle distribution is expressed as $f = f_0 + \delta f$. Here we separate the turbulence perturbation δf from the equilibrium distribution f_0 . In the electrostatic limit, the ion gyro-kinetic equation for δf_i , with μ and v_\parallel as independent velocity variables, is

$$\begin{aligned} &\frac{\partial \delta f_i}{\partial t} + (v_\parallel \hat{b} + \mathbf{v}_{E_0} + \mathbf{v}_E + \mathbf{v}_d) \cdot \nabla \delta f_i \\ &- \hat{b}^* \cdot \nabla \left(\mu B + \frac{e}{m_i} \Phi_0 + \frac{e}{m_i} \tilde{\phi} \right) \frac{\partial \delta f_i}{\partial v_\parallel} \\ &= -\mathbf{v}_E \cdot \nabla f_0 + \hat{b}^* \cdot \nabla \left(\frac{e}{m_i} \tilde{\phi} \right) \frac{\partial f_0}{\partial v_\parallel} + C_i^l(\delta f_i). \end{aligned} \quad (13)$$

Here, \mathbf{v}_{E_0} and \mathbf{v}_E are the $\mathbf{E} \times \mathbf{B}$ drift velocities corresponding to the equilibrium potential Φ_0 and the fluctuation potential $\tilde{\phi}$, respectively, \mathbf{v}_d is the ∇B drift velocity, $\hat{b}^* = \hat{b} + \rho_i \hat{b} \times (\hat{b} \cdot \nabla \hat{b})$, where $\hat{b} = \mathbf{B}/B$, and C_i^l is the linearized Coulomb collision operator. Note that a parallel velocity nonlinearity term that is one order higher³⁰ is retained in the equation. This term is required in order to maintain energy conservation.^{31,32} The equilibrium distribution function f_0 is determined by the neoclassical dynamics and obeys

$$\begin{aligned} &\frac{\partial f_0}{\partial t} + (v_\parallel \hat{b} + \mathbf{v}_{E_0} + \mathbf{v}_d) \cdot \nabla f_0 - \hat{b}^* \cdot \nabla \left(\mu B + \frac{e}{m_i} \Phi_0 \right) \frac{\partial f_0}{\partial v_\parallel} \\ &= C_i(f_0, f_0). \end{aligned} \quad (14)$$

The lowest-order solution of Eq. (14) is a shifted Maxwellian consistent with plasma rotation:

$$f_0 = f_{SM} = n(r, \theta) \left(\frac{m_i}{2\pi T_i} \right)^{3/2} e^{(-m_i/T_i)[(1/2)(v_\parallel - U_i)^2 + \mu B]}, \quad (15)$$

where the parallel flow velocity U_i is associated with the toroidal rotation by $U_i = I\omega_t/B$, where ω_t is the toroidal angular velocity, I is the toroidal current, and $n(r, \theta)$ is the ion density; namely, $n(r, \theta) = N(r) e^{m_i U_i^2 / 2T_i - e\tilde{\Phi}_0 / T_i}$. The total equi-

librium potential consists of two parts: $\Phi_0 = \langle \Phi_0 \rangle + \tilde{\Phi}_0$. Here, $\langle \rangle$ denotes a flux surface average. The poloidally varying component $\tilde{\Phi}_0$ can be generated by the centrifugal force, which drives charge separation on a magnetic surface in strongly rotating plasmas.³⁷ Generally the radial potential $\langle \Phi_0 \rangle$ is dominant. The equilibrium radial electric field can be calculated from a first-principles based particle simulation of neoclassical dynamics with important finite orbit effects,^{38,39} or obtained by direct experimental measurement if available. For equilibrium toroidal plasmas, a shifted Maxwellian with either model or experimental profiles of $\langle n(r, \theta) \rangle$, $T_i(r)$, and $\omega_i(r)$ is prescribed for the ions. The electron dynamics is described by the drift kinetic equation, neglecting the finite gyro-radius effect. The electron guiding center distribution is represented as $f_e = f_{e0} - (e\delta\phi/T_e)f_{e0} + \delta h_e$, with turbulence potential $\delta\phi = \phi - \langle \phi \rangle$. The equilibrium distribution f_{e0} satisfies the electron version of Eq. (14) and can be approximated by a shifted Maxwellian containing a parallel flow, similar to that for the ions. The second term for f_e represents the adiabatic electron response to the potential fluctuation due to the fast electron motion. The nonadiabatic electron distribution δh_e is determined by

$$\begin{aligned} & \frac{\partial \delta h_e}{\partial t} + (v_{\parallel} \hat{b} + \mathbf{v}_{E_0} + \mathbf{v}_E + \mathbf{v}_d) \cdot \nabla \delta h_e \\ & - \hat{b}^* \cdot \nabla \left(\mu B + \frac{e}{m_e} \Phi_0 + \frac{e}{m_e} \phi \right) \frac{\partial \delta h_e}{\partial v_{\parallel}} \\ & = - \mathbf{v}_E \cdot \nabla f_{e0} + \hat{b}^* \cdot \nabla \left(\frac{e}{m_e} \phi \right) \frac{\partial f_{e0}}{\partial v_{\parallel}} + \frac{e}{T_e} \frac{\partial \delta \phi}{\partial t} f_{e0} \\ & + (v_{\parallel} \hat{b} + \mathbf{v}_{E_0} + \mathbf{v}_E + \mathbf{v}_d) \cdot \nabla \left(\frac{e \delta \phi}{T_e} \right) f_{e0} + C_e^l(\delta h_e). \end{aligned} \quad (16)$$

Again, the parallel velocity nonlinearity is retained here for δh_e . At present, the trapped electron dynamics described by Eq. (16) is treated as a higher-order correction to the adiabatic response via a hybrid model^{40,41} in the electrostatic limit. To include full electron dynamics, we will use the split-weight scheme^{42,43} to solve Eq. (16).

The electrostatic fluctuation potential is divided into a turbulence part plus a zonal flow part: $\phi = \delta\phi + \phi_{00}$ with $\phi_{00} \equiv \langle \phi \rangle$. This expression emphasizes the critical role of turbulence-generated zonal flow in determining the turbulence and the associated transport level. For the turbulence potential, the gyro-kinetic Poisson equation¹⁶ becomes

$$\left(1 + \frac{T_i}{T_e} \right) \frac{e \delta \phi}{T_i} - \frac{e \tilde{\delta \phi}}{T_i} = \frac{\delta \bar{n}_i - \langle \delta \bar{n}_i \rangle}{n_0} - \frac{\delta n_e^{(1)} - \langle \delta n_e^{(1)} \rangle}{n_0}, \quad (17)$$

where $\delta \bar{n}_i$, expressed by Eq. (6), is the ion fluctuation density of guiding centers and $\delta n_e^{(1)} = \int d^3 v \delta h_e$ is the nonadiabatic density of electrons. Because the zonal flow has a larger spatial scale than the turbulence fluctuations, it is advantageous to solve for it separately in our simulations. The generalized equation for zonal flow in shaped geometry is obtained as

$$\begin{aligned} & \frac{1}{\mathcal{V}'_r} \frac{d}{dr} \left[\frac{d\phi_{00}}{dr} \mathcal{V}'_r \langle g^{rr} \rangle \right] \\ & = \frac{1}{\mathcal{V}'_r} \frac{d}{dr} \left\{ \frac{d}{dr} \left[\frac{T_i}{e} \left(\frac{\langle \delta \bar{n}_i \rangle}{n_0} - \frac{\langle \delta n_e^{(1)} \rangle}{n_0} \right) \right] \mathcal{V}'_r \langle g^{rr} \rangle \right\} \\ & - \left\langle \frac{1}{\rho_i^2} \right\rangle \frac{T_i}{e} \left(\frac{\langle \delta \bar{n}_i \rangle}{n_0} - \frac{\langle \delta n_e^{(1)} \rangle}{n_0} \right), \end{aligned} \quad (18)$$

where $\mathcal{V}'_r = \oint d\theta d\varphi \mathcal{J}$. In Eq. (18), we use the Padé approximation $\Gamma_0(b) \equiv I_0(b)e^{-b} \approx 1/(1+b)$ with I_0 the modified Bessel function and $b = (k_{\perp} \rho_i)^2$, and $\langle \tilde{\phi} \rangle \approx \langle \phi \rangle$. The latter approximation is not well justified for low-aspect-ratio geometry. A generalized field solver such as in Ref. 44 may help to remove this approximation.

III. SIMULATION RESULTS

The general geometry model has been implemented based on GTC architecture. In this section we present simulation results, including linear and nonlinear benchmarks, nonlocal ITG instability, nonlinear turbulence spreading in a shaped plasma, and turbulence self-regulation in a collisionless plasma.

A. Benchmarks

The general geometry model and simulation have been benchmarked, in the large-aspect-ratio circular concentric geometry limit, against the original GTC code, which uses a simple analytical MHD equilibrium. For this benchmark, a corresponding numerical equilibrium is produced for the general geometry simulation. The numerical equilibrium includes a mild Shafranov shift due to nonzero plasma beta and higher order (in the small inverse aspect ratio) corrections. The benchmarks are carried out for ion temperature gradient modes with a simplified adiabatic response for the electron dynamics. The representative parameters for the familiar Cyclone case¹⁰ are used here: inverse aspect ratio $a/R_0 = 0.358$, ion temperature profile $R_0/L_T = 6.92 \exp\{-(r-0.5)/0.28\}$,⁶ $T_e/T_i = 1$, $q = 0.854 + 2.184r^2$, and $L_T/L_n = 0.319$. For these simulations, as well as nonlinear simulations in Secs. III B and III C, no source is used, either based on artificially maintaining the plasma profile or modeling external particle and energy sources.

The linear benchmark simulations are carried out in a radial domain from 0.2 to 0.8 (in terms of normalized minor radius). In the toroidal direction, all simulations, including nonlinear runs in later sections, are run as a full torus (not a wedge). Additional parameters are: $a/\rho_i = 125$, total number of grid points is 1.5×10^6 with 32 poloidal planes, and less than five particles/cell are used in the linear simulation. The ITG instability is measured at $r = 0.5$, where the temperature gradient peaks. In each linear run, only a single- n mode with specified toroidal mode number is calculated using a filter process. Here, we specify five toroidal mode numbers: $n = 5, 9, 16, 23, 27$, which cover the poloidal wave numbers $k_{\theta} \rho_i$ from 0.1 to 0.6. As illustrated in Fig. 4, good agreement is obtained for the real frequencies ω_r , while the growth rates γ of the higher- n modes from the general ge-

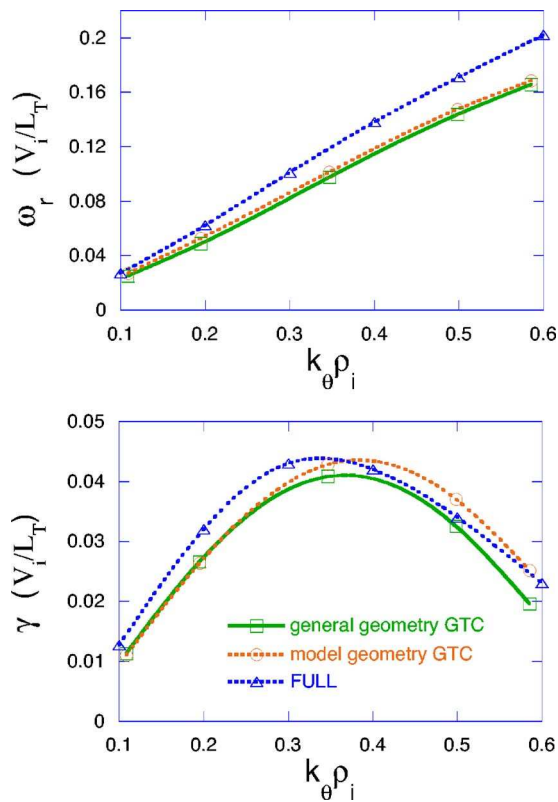


FIG. 4. (Color online) Real frequency ω_r and growth rate γ of ITG instability versus poloidal wave number k_θ , compared with the original GTC calculation and FULL code.

ometry simulation are slightly lower. The overall difference in frequency magnitude $|\omega|$ is less than 5%. The contour plots of the electrostatic potential perturbation on a poloidal plane show quite similar eigenmode structures from the two simulations. The ITG real frequencies and growth rates from our global simulations are also compared with local calculations using a comprehensive linear eigenvalue FULL code,^{45,46} and reasonably good agreement is obtained. It is noticed that the growth rates of our linear benchmark results agree reasonably well with previous benchmarks.¹⁰ However, the real frequencies are about 20% lower than that of the previous benchmarks. There are two major factors that may contribute to this difference. (i) The MHD equilibria are not identical for these simulations, which has considerable effects on ITG instability. The previous benchmarks used the so-called “ s - α ” model with $\alpha=0$. In our general geometry simulation, we use a numerical MHD equilibrium which has Shafranov shift due to nonzero plasma beta and includes finite-aspect-ratio corrections. These finite-aspect-ratio corrections are also taken into account in the analytic equilibrium used for the model geometry GTC simulation. It turns out that the linear frequency and growth rate are rather sensitive to these subtle differences of equilibrium. This is often observed in local linear calculations using the FULL code, and was also discussed in Ref. 19. (ii) There exist nonlocal effects in our global simulation, as suggested by the results presented in the next subsection.

The same parameters are used in the nonlinear ITG benchmark, except that the particle number per cell is in-

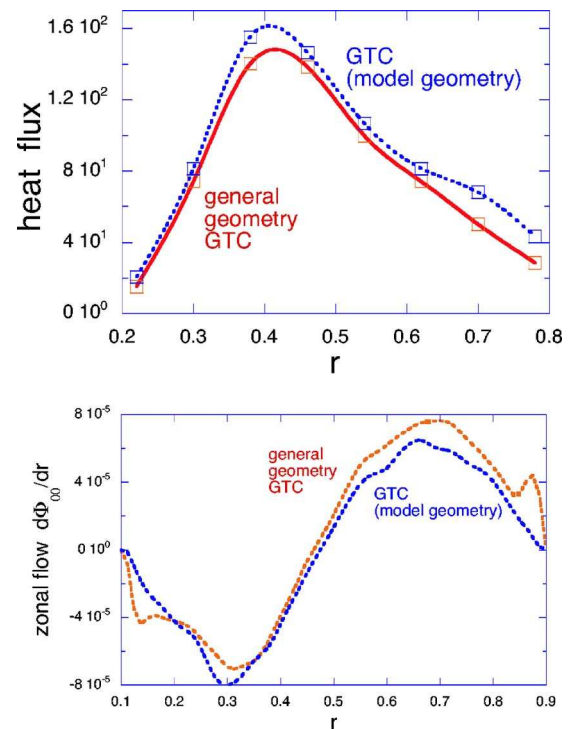


FIG. 5. (Color online) Steady-state heat flux profile and zonal flow profile of nonlinear ITG simulation with simple magnetic geometry, compared with the original GTC result.

creased to 20. The velocity space nonlinearity is included, which may have considerable effect on turbulence dynamics.⁴⁷ Flat marker temperature and density profiles are used in the general geometry GTC simulation for the benchmarks only. The radial simulation domain here is from $r=0.1$ to $r=0.9$. As shown in Fig. 5, the nonlinear benchmark results are in good agreement for both the steady-state heat flux and the zonal flow over the entire radial domain. It is also found that the self-generated zonal flow in ITG turbulence has a spatial scale of the order of the turbulence radial extension, with a roughly odd parity.

It is well known that electrostatic turbulence with adiabatic electrons does not drive particle transport across the magnetic field lines. This result can be used as a rigorous test for a complex simulation such as that developed in this paper. In Fig. 6 the heat flux, and the energy flux, which is the sum of the heat flux and the convective energy flux carried by the particle flux, versus time at $r=0.46$ are plotted. The result that the energy flux and heat flux are the same indicates that, indeed, no particle flux is produced in the simulation. Moreover, the particle flux is driven nowhere over the entire radial domain ($0.1 \leq r \leq 0.9$) of the global simulation.

The above linear and nonlinear benchmarks against the original GTC are nontrivial since, as detailed in Sec. II, the general geometry model and simulation are largely different in a number of aspects.

B. Nonlocal ITG modes and global turbulence dynamics

Most previous linear analysis of microinstability has been carried out locally, neglecting the radial variation of

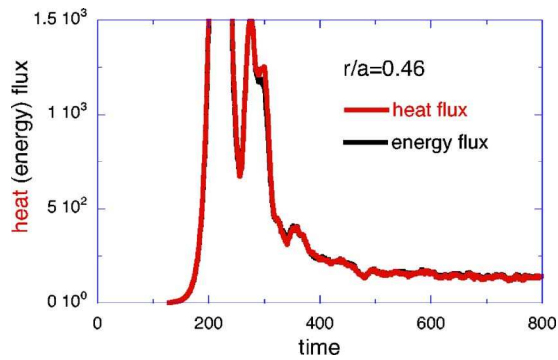


FIG. 6. (Color online) Temporal history of ion heat and energy flux of ITG turbulence with adiabatic electrons (from the simulation of the general geometry model).

equilibrium quantities such as pressure gradient and pressure itself. While GTC is a global toroidal code, in order to focus on the simplest problems involving shear effects due to the radial variation of the pressure gradient, the plasma temperature and density were assumed constant in the previous simulations. While such a treatment is well motivated and useful in separating and clarifying fundamental physics issues, it does not realistically capture the comprehensive global physics. In Fig. 7, we present an example of global ITG instability from the simulation of the general geometry model, taking into account the radial variation of temperature and density consistent with their gradient profiles. Corresponding to the temperature profile of Fig. 7, the system size is $a/\rho_i \approx 100$ (on average), and the simulation uses 1.5×10^6 grid points with less than five particles per cell. Compared to the simulation with constant T and n , the ITG growth rate is considerably reduced, with no significant change in the real frequency. Meanwhile, the contour plot of the electric potential on a poloidal plane shows that the eigenmode structure is twisted in the poloidal direction. Note that in this simulation and in nonlinear simulations hereafter, the nonuniform grid cells described in Sec. II A are used. The nonuniform grid cells, in general, are quite useful for experimental plasma profiles with substantial variation in temperature from the core to the edge, as they provide a roughly uniform (and efficient) spatial resolution in which the grid size is correlated with the local gyro-radius. For the cases simulated here, the benefit of nonuniform grid cells is less pronounced as the ratio of maximum to minimum gyro-radii is mild.

We have also applied our new nonlinear ITG simulation capability to a shaped toroidal plasma, based on the DIII-D experiment with the same model profiles as in Fig. 7. Additional parameters used in nonlinear simulations here and hereafter are: aspect ratio $R_0/a=3$, average $a/\rho_i \approx 200$, $T_e/T_i=1$, total grid points are about 1.2×10^7 with 64 poloidal planes, and average particle-number/cell is about 15. First, we examine the global turbulence evolution dynamics. The spatio-temporal evolution of the flux surface averaged turbulence intensity is plotted in Fig. 8. The turbulence is driven by the ion temperature gradient initially in the linearly unstable region ($0.42 < r < 0.76$), and then fluctuations spread in both the inward and outward radial directions to the linearly stable regions, leading to radially global turbu-

lence and transport nonlocality. The fluctuation intensity level in the stable regions is comparable to that in the original unstable regions. Also presented are three snapshots of the electric potential contour plot on a poloidal plane, which illustrate the dynamic, global evolution of turbulence. At an early time before the nonlinear saturation, radially elongated streamers are generated in the linearly unstable region with small extension into the linearly stable zone via linear toroidal coupling.⁴⁸ Later on, turbulence eddies are broken up by the self-generated $\mathbf{E} \times \mathbf{B}$ shearing flows (zonal flows) during the nonlinear saturation phase. A fast radial expansion of the fluctuations, with associated nonlinear toroidal coupling, immediately follows as the streamers are broken into smaller radial scale (higher radial wave number) fluctuations by the zonal flows. At a later time, they evolve into widely spread global turbulence, establishing the coupling between linearly stable and unstable regions.

Turbulence spreading has been widely observed in previous simulations. It is important to distinguish the turbulence spreading observed in a simulation from the possibility that initially locally stable regions may become unstable due to radial profile relaxation which may occur on the transport time scale. First, in our global simulation, the primary, most significant turbulence spreading is observed to occur right after the saturation of the linear ITG instability,⁴⁹ a quite short time scale on which the profile relaxation is negligible. Second, the k -spectrum of the spreading fluctuations observed in the linearly stable region shows significant differences from that of the ITG eigenmodes: the k_θ spectra are significantly down-shifted relative to those of unstable ITG modes, and there is no radially elongated eigenmode structure,⁴⁹ which is always observed in the linear phase of ITG-driven instability. These results will be published with more detail elsewhere in a separate paper.

C. Turbulence self-regulation in collisionless plasma

One of the key components in ITG turbulence is the zonal flow, which regulates the turbulence level locally.⁵⁰ Figure 9 illustrates the mutual self-regulation between the zonal flow and the turbulence. There exists a threshold for zonal flow excitation and a complex causal relation between the turbulence and the zonal flow. In this collisionless simulation, the observed oscillations in turbulence intensity and zonal flow energy can be generally attributed to the nonlinear interplay process in which the turbulence drives the zonal flow which, in turn, reduces the turbulence to a lower level. These oscillations should not be confused with the faster oscillations associated with the geodesic acoustic modes. It should be pointed out that the nonlinear oscillation shown here is different than that previously observed in Ref. 17, which is associated with the collisional damping of zonal flow.⁵¹

When the zonal flows are artificially excluded, our simulation shows that turbulence intensity does not oscillate after saturation. This clearly indicates that the oscillation behavior results from nonlinear interplay between turbulence and zonal flows. Note that similar properties for the zonal flow and drift wave system have been demonstrated in simple

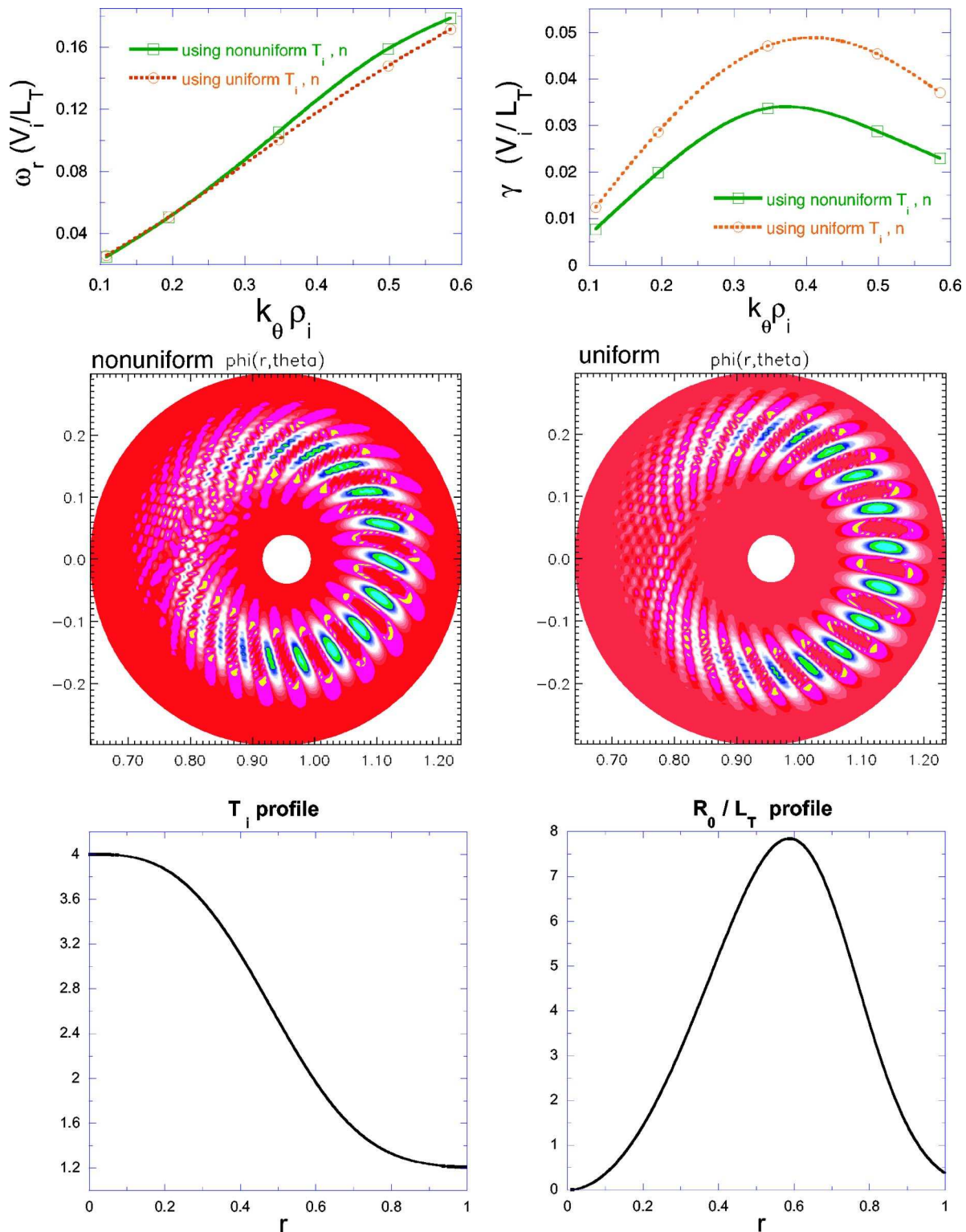


FIG. 7. (Color online) Simulation results of a nonlocal ITG instability using radially varying temperature and density, compared with the simulation neglecting the effects of radial shear of temperature and density: real frequency ω_r (upper-left) and growth rate γ (upper-right) vs $k_\theta \rho_i$; contour plot of electric potential from simulation with nonuniform T and n (middle-left) and simulation without the effects of T and n shear (middle-right); ion temperature profile (lower-left), and corresponding gradient profile (lower-right) used in the simulations.

analytical models^{52,53} in which, however, only the collisional damping of zonal flow is explicitly assumed. Here, the nonlinear oscillations shown in Fig. 9 occur with collisionless zonal flows. The apparent nonlinear collisionless damping processes, which are responsible for the saturation of zonal

flows and the nonlinear oscillations shown in Fig. 9, are not theoretically understood yet. The candidates may include the “tertiary instability,”⁵⁴ the generalized Kelvin-Helmholtz instability,⁵⁵ and the energy transfer to parallel sound waves and turbulence via poloidally asymmetric pressure

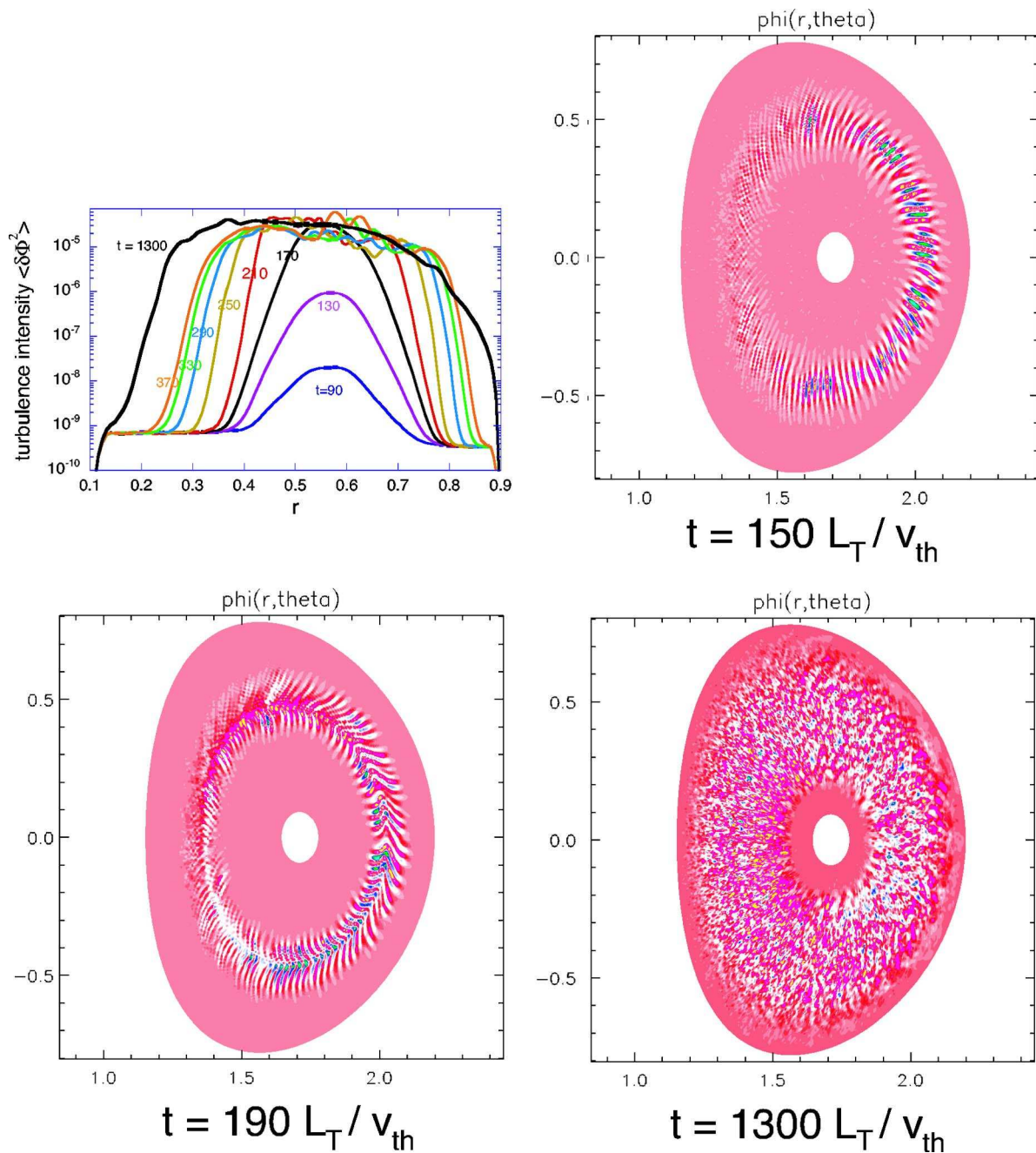


FIG. 8. (Color online) Spatio-temporal evolution of flux surface averaged turbulence intensity (upper left), and three snapshots of contour plot of electric potential on a poloidal plane from a simulation of a shaped plasma with typical DIII-D parameters.

perturbations,⁵⁶ etc.

Next, we attempt to clarify the possibility of energy transfer from zonal flow back to turbulence. In a consistent simulation, it is hard to identify this process from the entire nonlinear evolution of the system. Here we perform a carefully designed numerical experiment to examine this process. The simulation uses the same parameters as in Fig. 8. We introduce artificial zonal flows in the regions where the ITG mode is linearly (and also nonlinearly) stable ($r < 0.42$ and $r > 0.76$). The artificial zonal flows are driven by adding in Eq. (18) a nonzero axisymmetric density fluctuation $\langle \delta \bar{n}_i \rangle / n_0$, which is a certain fraction of that in the unstable region ($0.42 < r < 0.76$). In detail, we first calculate a non-

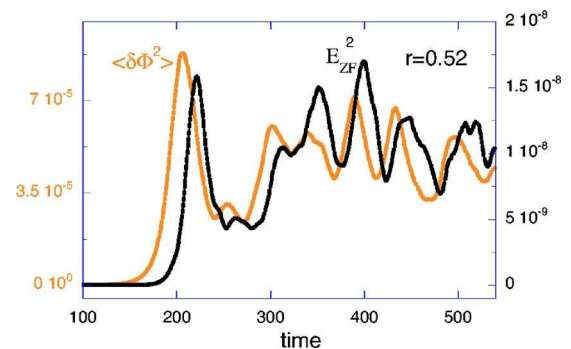


FIG. 9. (Color online) Temporal evolution of turbulence intensity $\langle \delta\Phi^2 \rangle$ and zonal flow energy $E_{ZF}^2 \propto |d\phi_0/dr|^2$ at $r=0.52$ (from the same simulation as Fig. 8).

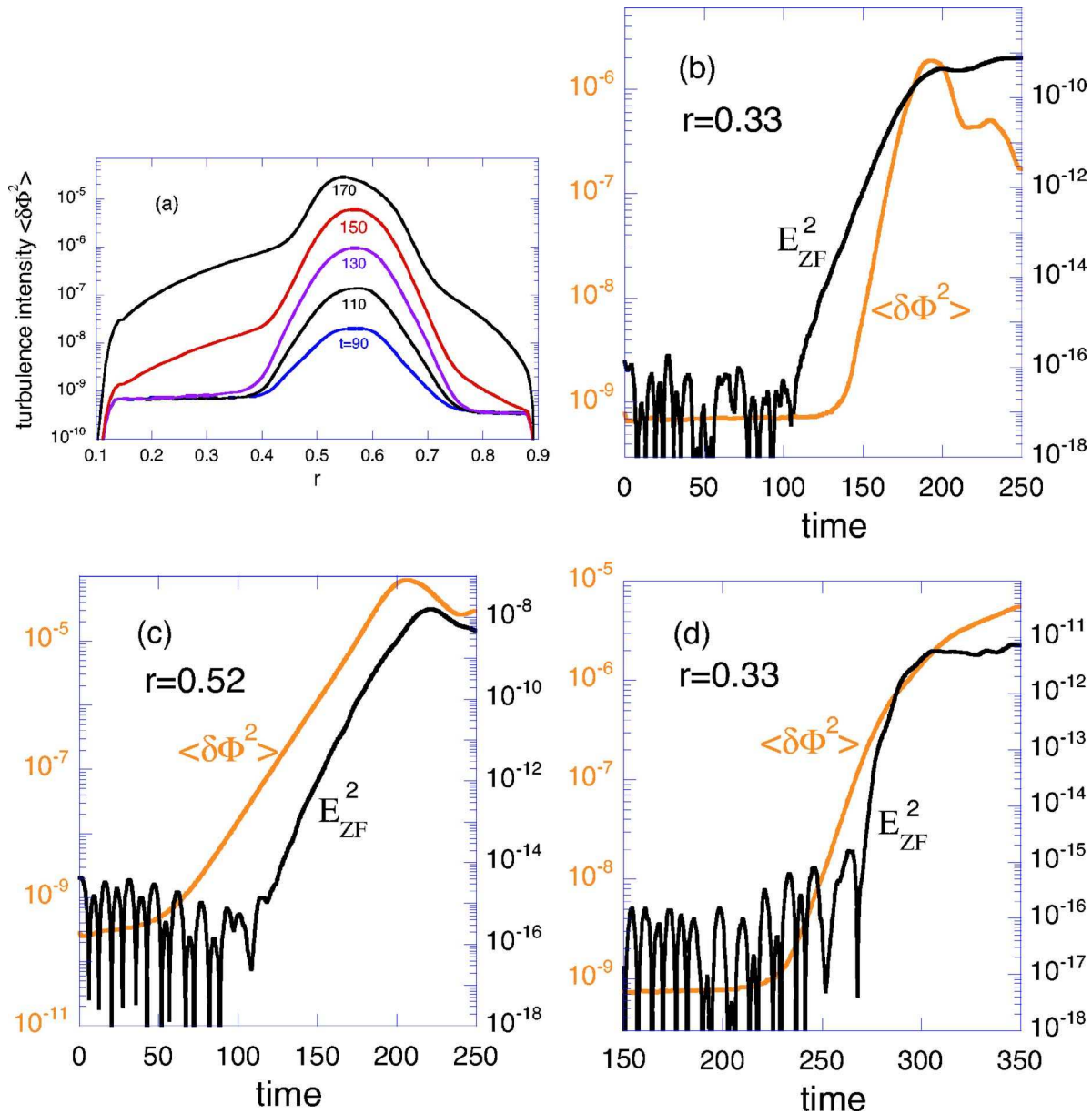


FIG. 10. (Color online) (a) Spatio-temporal evolution of turbulence intensity $\langle \delta\Phi^2 \rangle$ from a simulation with artificial zonal flows introduced in the ITG-stable regions $r < 0.42$ and $r > 0.76$; (b) temporal evolution of zonal flow energy $E_{ZF}^2 \propto |d\phi_{00}/dr|^2$ and turbulence intensity at an ITG stable location $r = 0.33$; temporal evolution of zonal flow energy and turbulence intensity at (c) $r = 0.52$ (linearly unstable region); and (d) $r = 0.33$ (linearly stable region) from the self-consistent simulation of Fig. 8.

zero density fluctuation in terms of $\langle \delta \bar{n}_i \rangle$ inside the unstable region via $\delta N_{00}(t) = \int_{r_1}^{r_2} \langle \delta \bar{n}_i \rangle V_r' dr$. Then δN_{00} is distributed into the ITG-stable region according to a given function $h(r) = \exp\{-[(r-r_c)/r_w]^\alpha\}$ with appropriate normalization. The local zonal flow pressure perturbation is also included. In this way it is related to the unstable region; the artificial zonal flow is excited simultaneously and can be saturated at roughly the same level as in the unstable region. The spatio-temporal evolution of the turbulence intensity is plotted in Fig. 10(a). Compared to the previous simulation of Fig. 8, this shows that, in the presence of artificial zonal flows, potential fluctuations are driven to grow in the regions where the ITG is stable. This fluctuation growth in the early phase occurs before the propagation front of ITG turbulence from the unstable region reaches the stable region. The temporal

evolution of zonal flow energy and turbulence intensity at $r = 0.33$ (ITG-stable region) plotted in Fig. 10(b) shows two interesting properties: (i) the turbulence components are temporally delayed relative to the zonal flow which is artificially excited at the same time as that in the unstable ITG region and (ii) there is an amplitude threshold for zonal flow to excite turbulence. Both are clear indications of a relation, that zonal flows can drive turbulence. This can be compared with the zonal flow generation process in the ITG-unstable region: Figure 10(c) shows that zonal flows are excited after the ITG driven turbulence grows to a certain level. As mentioned before, this simulation uses artificially driven zonal flows to demonstrate the possibility that zonal flows can drive turbulence, which would be difficult to identify in a self-consistent simulation with complex nonlinear dynamics.

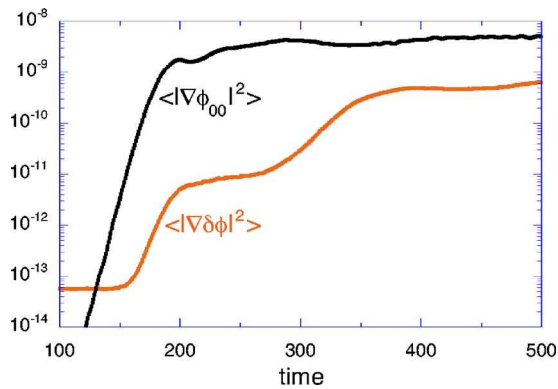


FIG. 11. (Color online) Temporal evolution of energy contained in artificial zonal flows and in driven turbulence at an ITG-stable location $r=0.33$.

It is also interesting to examine the zonal flow generation process in the ITG stable region in the consistent simulation of Fig. 8. The result here is presented in Fig. 10(d), which shows that zonal flows are excited by turbulence which has spread in.

After establishing the fact that zonal flows can drive turbulence, the next question is how efficiently can the energy be transferred from the zonal flows to the turbulence. Figure 11 shows the temporal evolution of zonal flow energy $\langle |\nabla\phi_{00}|^2 \rangle$, and turbulence energy $\langle |\nabla\delta\phi|^2 \rangle$. It is found that the saturated turbulence energy is two orders of magnitude smaller than that of the zonal flows. Note that, in Fig. 11, the second growth in turbulence energy, starting at $t \sim 270$, is caused by the spreading of the ITG-driven turbulence originating in the region $0.42 < r < 0.76$. Our numerical experiments also show that the above observations are not sensitive to the strength and the profile shape of the artificially excited zonal flows. In contrast, the zonal flow generation by the turbulence in the ITG-unstable region is very efficient in the sense that, during their generation process, zonal flows extract a large amount of energy from the turbulence components. Therefore, our simulation results suggest that zonal flows can drive turbulence. However, this process is too weak to be an effective zonal flow saturation mechanism.

It is noticed that this simulation result possesses some common features with previous simulations.⁵⁴ First, both simulations show that zonal flows can excite turbulence; second, the excited turbulence growth rate is comparable to and even larger than that of the ITG-driven turbulence. However, our simulation, in which both artificial zonal flows and their driven turbulence can reach saturation, also shows that the energy transfer from the zonal flows to the turbulence is small. As for this aspect, it was not reported in the previous study, which addressed mainly the zonal flow stability issue. Also note that direct comparison is difficult for these two very different simulations. The previous study was carried out using flux-tube simulation in the regime close to or slightly above the marginal ITG value (Dimits-shift regime¹⁰). Our study uses global simulation with artificial zonal flows excited in the linearly stable regime below marginal stability.

IV. SUMMARY

We have presented a generalized model that incorporates important realism of tokamak experiments into nonlinear gyro-kinetic simulations of plasma turbulence. These include a systematic treatment of plasma rotation and equilibrium $\mathbf{E} \times \mathbf{B}$ flow, realistic plasma profiles and corresponding MHD equilibria. The general geometry simulation capability has been developed with the following favorable features. (i) By rescaling the radial coordinate, the grid size in the perpendicular direction is correlated with the local gyro-radius which, varying substantially from the core to the edge, defines the spatial scale of turbulence at different locations. (ii) Gyro-kinetic transformations of potential and charge density between particle and guiding center positions are calculated with a finite ratio (B_θ/B) correction that is a significant geometry effect on the turbulence calculation, particularly for spherical torus devices. (iii) The applied equilibrium $\mathbf{E} \times \mathbf{B}$ flow with the spatial scale of the plasma minor radius, which is believed to play an important role in determining the turbulence level, is calculated from our first-principles based particle simulation of global neoclassical dynamics with important finite orbit effects. Working with a symmetry coordinate system, we can construct a relatively regular mesh in real space for strongly shaped toroidal plasmas. This also facilitates straightforward visualization. In the large-aspect-ratio circular concentric geometry limit, cross benchmarks of the linear and nonlinear characteristics, such as real frequency, growth rate, steady-state heat flux, and zonal flow amplitude of ITG turbulence have been carried out to validate the general geometry model and simulation.

Our nonlinear simulations have been applied to a DIII-D-shaped plasma to examine both local and nonlocal phenomena of ITG turbulence. The dynamic evolution from the radially elongated streamers generated by localized instability, to short radial scale fluctuations due to the shearing decorrelation of the zonal flows, and then to radially global turbulence via turbulence spreading into linearly stable regions, has been demonstrated. The coupling established between linearly stable and unstable regions via turbulence spreading, as shown in our simulation, may explain some experimental reports of the existence of finite density fluctuations and anomalous heat transport in the linearly stable region inside an internal transport barrier.⁵⁷ With regard to the nonlinear interplay between zonal flow and turbulence, our numerical experiments suggest that the zonal flows can drive turbulence. However, the associated energy coupling is too weak to provide sufficient zonal flow damping to be responsible for zonal flow saturation and the bursting behavior in the fluctuations observed in our collisionless simulations.

ACKNOWLEDGMENTS

The authors would like to acknowledge Dr. R. White and Dr. L. Zharov for help with the MHD equilibrium interface and useful discussions, and Dr. A. Boozer, Dr. L. Chen, Dr. P. Diamond, Dr. R. Goldston, Dr. F. Hinton, Dr. R. Nazikian, Dr. Y. Nishimura, and Dr. X. Tang for valuable discussions.

This work was supported by the U.S. Department of Energy (DOE) Scientific Discovery through Advanced Comput-

ing (SciDAC) Center for Gyrokinetic Particle Simulation, and by DOE Contract No DE-AC02-CHO-3073.

- ¹W. M. Tang, Nucl. Fusion **18**, 1089 (1978).
- ²J. W. Connor and H. R. Wilson, Plasma Phys. Controlled Fusion **36**, 719 (1994).
- ³W. Horton, Rev. Mod. Phys. **71**, 735 (1999).
- ⁴S. Parker, W. Lee, and R. Santoro, Phys. Rev. Lett. **71**, 2042 (1993).
- ⁵M. Kotschenreuther, G. Rewoldt, and W. M. Tang, Comput. Phys. Commun. **88**, 128 (1995).
- ⁶R. D. Sydora, V. K. Decyk, and J. M. Dawson, Plasma Phys. Controlled Fusion **38**, A281 (1996).
- ⁷M. A. Beer and G. W. Hammett, Phys. Plasmas **3**, 4046 (1996).
- ⁸Z. Lin, T. S. Hahm, W. W. Lee, W. M. Tang, and R. White, Science **281**, 1835 (1998).
- ⁹W. Dorland, B. N. Rogers, F. Jenko *et al.*, Proc. 18th Intl. Conf. on Fusion Energy, Sorrento, Italy, 2000 (International Atomic Energy Agency, Vienna), paper TH2/5.
- ¹⁰A. M. Dimits, G. Bateman, M. A. Beer *et al.*, Phys. Plasmas **7**, 969 (2000).
- ¹¹F. Jenko, Comput. Phys. Commun. **125**, 196 (2000).
- ¹²J. Candy and R. Waltz, J. Comput. Phys. **186**, 545 (2003).
- ¹³Y. Chen and S. Parker, J. Comput. Phys. **189**, 463 (2003).
- ¹⁴Y. Idomura, S. Tokuda, and Y. Kishimoto, Nucl. Fusion **43**, 243 (2003).
- ¹⁵L. Villard, S. J. Allfrey, A. Bottino *et al.*, Nucl. Fusion **44**, 172 (2004).
- ¹⁶W. W. Lee, Phys. Fluids **26**, 556 (1983).
- ¹⁷Z. Lin, T. S. Hahm, W. W. Lee, W. M. Tang, and P. H. Diamond, Phys. Rev. Lett. **83**, 3645 (1999).
- ¹⁸Z. Lin, S. Ethier, T. S. Hahm, and W. M. Tang, Phys. Rev. Lett. **88**, 195004 (2002).
- ¹⁹Z. Lin and T. S. Hahm, Phys. Plasmas **11**, 1099 (2004).
- ²⁰T. S. Hahm, P. H. Diamond, Z. Lin, K. Itoh, and S.-I. Itoh, Plasma Phys. Controlled Fusion **46**, 323 (2004).
- ²¹T. S. Hahm, P. H. Diamond, Z. Lin, G. Rewoldt, O. Gurcan, and S. Ethier, Phys. Plasmas **12**, 090903 (2005).
- ²²R. J. Goldston, *Basic Physical Processes of Toroidal Fusion Plasmas*, Proceedings of Course and Workshop, Varenna, 1985, edited by G. P. Lampis, M. Lontano, G. G. Leotta, A. Malein, and E. Sindoni (Monotypia Franchi, Citta di Castello, 1985), Vol. 1, p. 165.
- ²³J. DeLucia, S. C. Jardin, and A. M. M. Todd, J. Comput. Phys. **37**, 183 (1980).
- ²⁴L. E. Zakharov and A. Pletzer, Phys. Plasmas **6**, 4693 (1999).
- ²⁵J. Luxon, Nucl. Fusion **42**, 614 (2002).
- ²⁶M. Ono, S. M. Kaye, Y.-K. M. Peng *et al.*, Nucl. Fusion **40**, 557 (2000).
- ²⁷B. Scott, Phys. Plasmas **6**, 2334 (1998).
- ²⁸R. White and L. E. Zakharov, Phys. Plasmas **10**, 573 (2003).
- ²⁹R. J. Littlejohn, Phys. Fluids **24**, 1730 (1981).
- ³⁰E. A. Frieman and L. Chen, Phys. Fluids **25**, 502 (1982).
- ³¹D. H. E. Dubin, J. A. Krommes, C. Oberman, and W. W. Lee, Phys. Fluids **26**, 3524 (1983).
- ³²T. S. Hahm, Phys. Fluids **31**, 2670 (1988).
- ³³A. J. Brizard, J. Plasma Phys. **41**, 541 (1989).
- ³⁴T. S. Hahm, Phys. Plasmas **3**, 4658 (1996).
- ³⁵W. W. Lee, J. Comput. Phys. **72**, 243 (1987).
- ³⁶Z. Lin and W. W. Lee, Phys. Rev. E **52**, 5646 (1995).
- ³⁷F. L. Hinton and S. K. Wong, Phys. Fluids **28**, 3028 (1985).
- ³⁸W. X. Wang, F. L. Hinton, and K. Wang, Phys. Rev. Lett. **87**, 055002 (2001).
- ³⁹W. X. Wang, W. M. Tang, F. L. Hinton, L. E. Zakharov, R. B. White, and J. Manickam, Comput. Phys. Commun. **164**, 178 (2004).
- ⁴⁰Z. Lin and L. Chen, Phys. Plasmas **8**, 1447 (2001).
- ⁴¹W. X. Wang, L. Chen, and Z. Lin, Bull. Am. Phys. Soc. **46**, 114 (2001).
- ⁴²I. Manuilskiy and W. W. Lee, Phys. Plasmas **7**, 1381 (2000).
- ⁴³J. L. V. Lewandowski, Phys. Plasmas **10**, 3204 (2003).
- ⁴⁴Y. Nishimura, Z. Lin, J. L. V. Lewandowski, and S. Ethier, J. Comput. Phys. **214**, 657 (2006).
- ⁴⁵G. Rewoldt, W. M. Tang, and M. S. Chance, Phys. Fluids **25**, 480 (1982).
- ⁴⁶G. Rewoldt, W. M. Tang, and R. J. Hastie, Phys. Fluids **30**, 807 (1987).
- ⁴⁷W. W. Lee, Bull. Am. Phys. Soc. **49**(8), 135 (2004).
- ⁴⁸X. Garbet, L. Laurent, A. Samain, and J. Chinardet, Nucl. Fusion **34**, 963 (1994).
- ⁴⁹W. X. Wang, Bull. Am. Phys. Soc. **50**, 180 (2005).
- ⁵⁰P. H. Diamond, K. Itoh, S.-I. Itoh, and T. S. Hahm, Plasma Phys. Controlled Fusion **47**, R35 (2005).
- ⁵¹F. L. Hinton and M. N. Rosenbluth, Plasma Phys. Controlled Fusion **41**, A653 (1999).
- ⁵²M. A. Malkov, P. H. Diamond, and M. N. Rosenbluth, Phys. Plasmas **8**, 5073 (2001).
- ⁵³R. White, L. Chen, and F. Zonca, Phys. Plasmas **12**, 057304 (2005).
- ⁵⁴B. N. Rogers, W. Dorland, and M. Kotschenreuther, Phys. Rev. Lett. **85**, 5336 (2000).
- ⁵⁵E. J. Kim and P. H. Diamond, Phys. Plasmas **9**, 4530 (2002).
- ⁵⁶N. Miyato, Y. Kishimoto, and J. Li, Phys. Plasmas **12**, 5557 (2004).
- ⁵⁷R. Nazikian, K. Shinohara, G. J. Kramer *et al.*, Phys. Rev. Lett. **94**, 135002 (2005).